Estimation of the biomechanical mammographic deformation of the breast using machine learning models

S. Said[a], Z. Yang[a,c], P. Clauser[b], N.V. Ruiter[a], P.A.T. Baltzer[b] and T. Hopp[a]

[a]Karlsruhe Institute of Technology (KIT), Institute for Data Processing and Electronics, Karlsruhe, Germany
[b]Medical University of Vienna, Department of Biomedical Imaging and Image-guided Therapy, Vienna, Austria
[c]Medical Faculty Mannheim - Heidelberg Universtiy Computer Assisted Clinical Medicine, Mannheim, Germany

ARTICLE INFO

Keywords:
Biomechanical Simulation
Breast Imaging
Mammographic Compression
Finite Element Methods
Machine Learning
Clinical Datasets

ABSTRACT

Background A typical problem in the registration of MRI and X-ray mammography is the nonlinear deformation applied to the breast during mammography. We have developed a method for virtual deformation of the breast using a biomechanical model automatically constructed from MRI. The virtual deformation is applied in two steps: unloaded state estimation and compression simulation. The finite element method is used to solve the deformation process. However, the extensive computational cost prevents its usage in clinical routine.

Methods We propose three machine learning models to overcome this problem: an extremely randomized tree (first model), extreme gradient boosting (second model), and deep learning-based bidirectional long short-term memory with an attention layer (third model) to predict the deformation of a biomechanical model. We evaluated our methods with 516 breasts with realistic compression ratios up to 76%.

Findings We first applied one-fold validation, in which the second and third models performed better than the first model. We then applied ten-fold validation. For the unloaded state estimation, the median RMSE for the second and third models is 0.8 mm and 1.2 mm, respectively. For the compression, the median RMSE is 3.4 mm for both models. We evaluated correlations between model accuracy and characteristics of the clinical datasets such as compression ratio, breast volume, and tissue types.

Interpretation Using the proposed models, we achieved accurate results comparable to the finite element model, with a speedup of factor 240 using the extreme gradient boosting model. These proposed models can replace the finite element model simulation, enabling clinically relevant real-time application.

1. Introduction

The second-leading cause of death in the United States and a major public health issue worldwide is cancer. In the United States, 1,918,030 new cancer cases and 609,360 cancer-related deaths were recorded in 2022. 43,250 and 530 female and male patients, respectively were expected to die from breast cancer out of 290,560 newly diagnosed cases. The incidence of breast cancer in women increased slowly by 0.5% per year from 2014 to 2018. Although incidence trends, and thereby mortality patterns for breast cancer are slowing, there has not been a dramatic decline despite the large efforts in early diagnosis. Investments in improved early diagnosis and treatment, as well as more focused cancer control initiatives, could reduce cancer mortality in the future Siegel et al. (2022).

There are several imaging techniques available for the detection and diagnosis of breast cancer, such as magnetic reasoning imaging (MRI), X-ray mammography, digital breast tomosynthesis, and ultrasound images. Imaging techniques often complement each other.

Due to different patient positioning and compression of the breast in those modalities, image registration is one of the methods that has been researched in the last decades to facilitate multimodality diagnosis by transferring lesion positions from one modality to another. The predominant challenge in breast image registration is the huge nonlinear deformation of soft tissue, e.g. when the breast is compressed in mammography. To overcome this challenge, the state of the art in multimodal breast image registration is the application of sophisticated biomechanical simulations, mostly solved with the finite element methods (FEM) García et al. (2018).

1.1. Finite Element Methods and Application to Biomechanical Breast Models

Finite Element Methods discretize an object to approximately solve the differential equations describing the physical conditions Pasciak (1995). The boundary conditions are considered as input from which the algorithm approximates to the corresponding solution Pasciak (1995). The continuum problem is approximated by a method where the continuum is partitioned into a finite number of elements and a finite set of parameters determines the performance of these elements. The solution of the whole system as a set of its elements pursues exactly the same principles that apply to standard discrete problems Zienkiewicz et al. (2013). Biomechanical modeling (BM) of the behavior of anatomical structures under different loads is a necessary step for numerous academic and clinical applications. Corresponding partial differential equations (PDEs) control the physical phenomenon being modeled such as the deformation of organs like liver, prostate, stomach, breast, and other

ORCID(s): https://orcid.org/0000-0002-7441-6135 (S. Said); https://orcid.org/0000-0002-4411-4056 (N.V. Ruiter); https://orcid.org/0000-0001-7324-1735 (T. Hopp)

Table 1
Literature review of finite element methods for breast deformation

Reference	Application	Compression Ratio	Computation Time	Software	Studies
Azar et al. (2000)	MR image-guided biopsy	12% - 26%	$<$ 30 mins	ABAQUS	Clincial
Samani et al. (2001)	Image registration	-	-	ABAQUS	Phantom
Ruiter et al. (2002)	Cancer diagnosis	21%	-	ANSYS	Clinical
Ruiter et al. (2006)	Image registration	6% -∼25%	-	ANSYS	Clinical
Tanner et al. (2006)	Breast deformation	20%	-	ANSYS	Clinical
Chung et al. (2008)	Image registration	30%	-	-	Phantom
Han et al. (2011b)	Breast deformation	19.4%-50.4%	312 mins (Explicit)	ABAQUS	Clinical
Hopp et al. (2013)	Image registration	∼50%	20 mins (Optim.:120 mins)	ABAQUS	Clinical
Lee et al. (2013)	Image registration	40% -70%	-	CMISS	Clinical
Mertzanidou et al. (2014)	Image registration	50%	2 hrs	ITK	Clinical
Liu et al. (2017)	Simulation compression	∼56%	-	ABAQUS	Clinical
García et al. (2019)	Image registration	-	61 min (Optim.)	NiftySim	Clinical

virtual organs in augmented reality applications Phellan et al. (2021).

FEM specifically for modeling the mechanical response of breast tissue have been used for several applications with different complexities of biomechanical models and materials Hipwell et al. (2016), García et al. (2018). More specifically, the mechanical response of breast tissue under mammographic compression has been modeled using FEM, using different compression ratios and different solvers. An overview of the compression ratios, software packages, computational time, and type of studies used is presented in Table 1.

Despite the fact that these models have been used with success to register multimodal breast images, FEM are time consuming and thus limit clinical applicability and integration into clinical workflows. Furthermore, several approaches consider an iterative scheme to optimize meta parameters such as compression thickness, material parameters, or breast rotation to cope with uncertainties in clinical data (referred to as "Optim." for optimization in Table 1). Therefore, the FEM simulation have to be computed numerous times, which increase further the overall computation time. The challenge of accurate real-time modeling of soft tissue deformation is still an open question.

Numerous strategies have been proposed to reduce the computational effort of FEM in order to achieve real-time compliance. Some of them focused on improving linear solvers, which are the main FEM bottleneck Mendizabal et al. (2019). The GPU implementation by Han et al. (2014) relies on a total lagrangian explicit dynamics (TLED) formulation by Miller et al. (2006), which is considered the most optimal method for modeling breast biomechanics Mendizabal et al. (2019). Moreover, niftySim is a GPU-based solver Han et al. (2011a), used for breast modeling. The Simulation Open Framework Architecture (SOFA) also uses a GPU-based solver to accelerate computations and has been used for prostate deformation simulation Moreira et al. (2013).

1.2. Machine and Deep Learning Algorithms

A lot of research has been done to predict the mechanical behavior of different anatomical structures using different machine learning algorithms Phellan et al. (2021). The fundamental benefit of ML models is their ability to forecast outcomes in real-time once the mapping function has been computed offline. The three main types of algorithms are neural networks (NNs), tree-based algorithms, and support vector regression (SVR) machines. Although many anatomical structures have been studied with machine learning Phellan et al. (2021), for simulating the deformation of the breast, to our best knowledge, there has been limited research:

Mendizabal et al. (2019) focused on simulating deformations of ultrasound images for ultrasound-guided breast biopsy. They used a U-net architecture trained on a small synthetic dataset. Their main goal was to find a relationship between the partial surface deformation under the US probe and the deformation inside the breast. For that purpose, they were able to make an accurate prediction for lesion displacement in real-time. Their model did not take into consideration the heterogeneity or complex boundary conditions that actually exist in clinical cases. Their model is insensitive to the patient-specific elastic properties because it only accounts for surface displacement.

For the evaluation, they used the displacements generated by the FEM as ground truth and then calculated the mean error. Since their goal was to accurately predict lesions, they also calculated the target registration error (TRE) between their prediction and the known lesion in the phantom breast. They used different probe displacements from less than 12.5 mm to more than 27.5 mm, achieving a mean TRE of 2.7 mm to 5.8 mm, respectively. Their main limitation was that they had to re-train the model for each new geometry, which is restricted to the types and number of compression tools such as different probe shapes Mendizabal et al. (2019).

Martínez-Martínez et al. (2017) and Rupérez et al. (2018) modeled the mechanical response of breast tissue under mammographic compression using an MRI-derived nonlinear finite element model. Their main goal was to

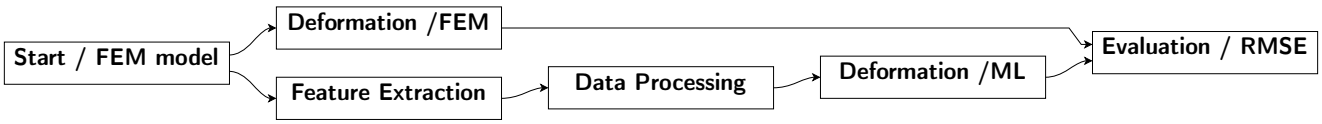

Figure 1: Workflow of our proposed method

accelerate the multimodal registration and simulate breast tissue behavior during image-guided interventions such as biopsies. They proposed three models: decision tree (DT), extremely randomized trees (ERT), and random forest (RF). They first conducted their experiments based on phantoms and then extended them to clinical datasets.

They evaluated their methods by calculating the mean 3D Euclidean distance between the nodes predicted by the models and the nodes extracted from the FE simulation, which served as the ground truth. Their experiments showed that ERT had the best performance with an average error of 0.62 mm. One limitation is the number of datasets (10 phantoms, 10 clinical cases) that were evaluated, which limits the generalization of the model. In addition, only a compression ratio of 20% was considered, which is much lower than the compression ratios applied in mammography. Their model consisted of three tissue types: fatty and glandular tissues and skin.

In this paper, we propose and compare two machine learning models, i.e. extremely randomized tree (ERT) and extreme gradient boosting (XGBoost), and a deep learning model (Att-BLSTM) to predict the deformation of a biomechanical model based on breast MRI under realistic mammographic compression. The biomechanical model is based on our previous work, see e.g. Hopp et al. (2012, 2013), which can be considered relatively complex as it considers four tissue types: fatty, glandular, and muscular tissues, as well as skin. Furthermore, it uses an estimation of the unloaded state of the breast before applying plate compression using a contact problem between the breast and the rigid compression plates.

The model has been evaluated in several clinical use cases and obtained clinically relevant results, e.g. for multimodal diagnosis of MRI and X-ray mammography with an average localization error of about 13 to 18 *mm* Dietzel et al. (2012); Hopp et al. (2013), image fusion of MRI contrast kinetics with X-ray mammograms Dietzel et al. (2015); Hopp et al. (2012), and for multimodal computer-aided diagnosis Hopp et al. (2017, 2016).

Based on the metadata of the corresponding mammograms of the patients included in this study, we considered compression ratios of up to 76%. We tested our ML and DL approaches with 516 breasts for which we automatically generated the biomechanical models from T2-weighted MR images. We trained and evaluated the models using a FEM simulation of mammographic compression and correlated the results with characteristics of the clinical datasets such as compression ratio, accuracy as a function of tissue type, and breast volume.

2. Methods

2.1. Biomechanical Breast Model

Our biomechanical breast model is based on the method of registration of MRI and full X-ray mammography developed in earlier work of our group Hopp et al. (2013). It estimates a configuration of the breast comparable to its shape in X-ray mammography based on the breast geometry observed with MRI in 3D. A biomechanical model is used in combination with a FEM simulation which virtually mimics the deformation applied to the MRI.

2.1.1. Image Segmentation and Meshes

To obtain the patient-specific breast geometry, we segmented a T2-weighted MR image using an unsupervised neural network (for details, please refer to Said et al. (2022)). It is based on an iterative method that generates various segmentations of the same MRI volume, from which we selected the presumably best segmentation based on independent quality metrics. Three main tissues are classified: fatty, glandular, and muscular tissues.

A tetrahedral meshing approach was used to construct the model geometry from the segmented MRI, which divides the breast anatomy into approximately $2000 \sim 2500$ 4-node tetrahedrons using the iso2mesh tool Fang and Boas (2009). This method is based on tetgen Si and Gärtner (2005) and CGAL The CGAL Project (2022). For details, please refer to Said et al. (2021).

2.1.2. Material Model and Boundary Conditions

An isotropic hyperelastic neo-Hookean material model was used to account for the nonlinear and incompressible tissue behavior during the deformation process Wellman et al. (1999). Two material constants C_{01} and D_1 are determined as functions of Young's modulus E and Poisson's ratio ν to describe the stress-strain relationship of the breast tissue. The values used are the same as in our previous work Said et al. (2021). Poisson's ratio ν was set to 0.495 for all three tissues while Young's modulus differed from one tissue to another. E_{fat} was set to 1100 Pa, E_{Gland} was set to 2500 Pa, and E_{Muscle} was set to 6000 Pa. On the top of the outer breast surface, we modeled a simplified layer of skin using membrane elements. The geometry of these membrane elements is a 3-node triangle with a constant thickness of 2 *mm* for all the clinical datasets. Similarly, a hyperelastic neo-Hookean material was used with E_{Skin} set to 1000 Pa. A more detailed description of the biomechanically based registration and the relationship between stresses and strains is discussed in Hopp et al. (2012).

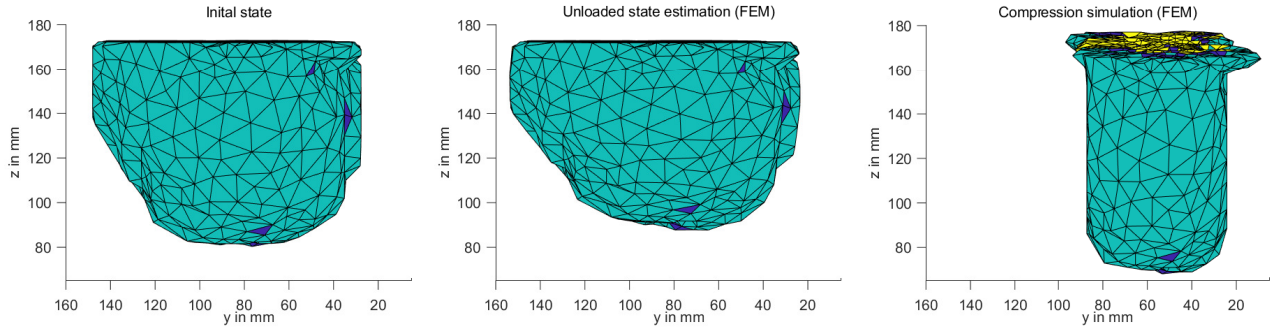

Figure 2: A clinical case of our biomechanical model in the sagittal plane (lateral view): The initial state, the unloaded state estimation followed by the compression step.

As for the boundary conditions, the breast was modeled as an adjunct to the body by considering the muscle as a non-deformable body. In the anteroposterior direction, we constrained the movement of nodes at the interface between the muscle and other tissues.

We mimicked mammographic compression in two steps: we first simulated the unloaded state of the breast in which no gravity is applied to the breast. This is modeled in a simplified way by applying a body force with a gravitational force in the anteroposterior direction. In the second simulation step, we added compression plates to compress the breast until the required compression thickness was achieved as shown in Figure 2. The compression thickness was read from the metadata. Our assumption was that the lower compression plate was fixed at the inframammary fold and only the upper plate moved toward the breast. In terms of boundary conditions, a displacement of the upper compression plate was defined and the lower plate was kept in position. We used 8-node hexahedrons to model the plates and applied a linear elastic material with material parameters mimicking acrylic glass. The deformation simulation of the breast was considered as a contact problem between the breast surface and the plate surfaces, defining a small sliding interface with an adjustable friction coefficient of 0.25. Due to the nearly incompressible material, the employed deformation mostly affected the shape of the breast and not a volume change.

We employed the FEM to compute the mechanical response of the breast tissue for the modeled compression. The mechanical deformations were estimated using the dynamic FE solver in the commercial FEM software ABAQUS / Explicit Smith (2009), which was selected for its robust convergence for highly nonlinear deformations and contact problems. The nonlinear system of equations is solved in ABAQUS / Explicit using a small-step incremental solution method. The simulation of the breast compression is divided into small time steps to calculate the displacements of the moving upper plate towards the breast. For each small time step, we took into consideration the geometric non-linearity of the breast. We used a smooth step displacement curve and set ABAQUS / Explicit to automatically determine the step size and convergence criterion of each increment. We can extract the deformed configuration of the breast by requesting from ABAQUS the node positions at a certain time step (referred to as "step number"). We used this information as a feature for training our ML models, as described in the next section.

2.2. Data Generation and Features Extraction

The extracted features mainly contain three different types of information: the geometry of the breast described by the initial coordinates of the breast mesh, the properties of the tissues such as the breast volume and the volume fractions of the tissues given by the segmentation, and the external factors causing the deformation such as the position of the compression plates and surface nodes of the breast mesh. As mentioned before, our biomechanical simulation consists of two steps: estimation of the unloaded state and simulation of the compression. For the estimation of the unloaded state, we extracted eleven features similar to those proposed in Martínez-Martínez et al. (2017); Rupérez et al. (2018). For the compression simulation, we extracted a total of 22 features: the same eleven features as in Martínez-Martínez et al. (2017); Rupérez et al. (2018) and an additional eleven features that empirically improved the results in our experiments, especially for the large deformations during the breast compression simulation. A description of the 22 features is summarized in the following list:

- Feature 1-3: The three components of the nodal coordinates (X, Y, and Z) of each node in the initial breast geometry
- Feature 4: The step number at which the nodal coordinate was acquired
- Feature 5-7: The volume fraction of each segmented tissue (fatty, glandular, and muscular tissues) compared to the total volume of the breast
- Feature 8: The volume of the breast mesh in mm^3
- Feature 9-11: The fraction of elements for each tissue type (fatty, glandular, and muscular tissues) compared to the total number of elements in the breast mesh

- Feature 12: The displacement of the upper compression plate towards the breast for the particular step
- Feature 13-14: Y and Z coordinates of the edge of the fixed lower compression plate
- Feature 15-16: Y and Z coordinates of the edge of the moving upper compression plate for the particular step
- Feature 17: a flag indicating if the node of the current instance is a surface node of the breast mesh which will potentially get into contact with the upper compression plate
- Feature 18: a flag indicating if the node of the current instance is a surface node of the breast. Note that these nodes are also the nodes forming the membrane elements modeling the skin.
- Feature 19-21: 3-bit binary value representation of the tissue type to which the node belongs based on the breast mesh as shown in Table 2
- Feature 22: Laterality of the breast mesh (left or right breast)

Finally, one instance of 22 features represents the information of one node in a breast.

Table 2
Tissue labels

bit 2	bit 1	bit 0	Class
0	0	1	muscle
0	1	0	fatty
0	1	1	interface (fatty, muscle)
1	0	0	glandular
1	0	1	interface (glandular, muscle)
1	1	0	interface (fatty, glandular)
1	1	1	interface (three tissues)

After extracting the features, we organized them in a 2D matrix where the columns represent 11 and 22 features for the unloaded state estimation and compression step, respectively and the rows represent the nodes at one time step as an instance as shown in Figure 3.

2.3. Data Processing

Before feeding the instances into the machine learning algorithms, we first applied a preprocessing step, which consists mainly of a normalization.

It is responsible for bringing different breast geometries into a similar reference space to increase robustness and training stability.

In our application, due to the large variance in the geometry of the breasts, such as position, shape, and size, normalization is an essential step to bring the plates and the breast mesh into the same coordinate system.

It has been empirically tested that the z-score normalization has the best performance for our problem: we performed

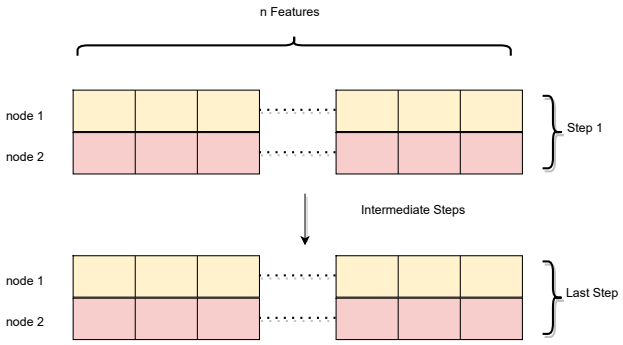

Figure 3: Data structure of the features, which are considered as the input for training our machine and deep learning models.

a pretest comparing two common normalization methods: z-score and min-max scaling normalization. A small dataset of 100 breasts was used for training and 10 breasts were predicted using our machine learning and deep learning models, which will be described in section 2.4. We evaluated the performance using the root mean square error (RMSE) (see section 2.5) and analyzed the percentages of nodes in the breast model with an RMSE less than 2 mm. For the z-score normalization on average 14.4% of the nodes had an RMSE less than 2 mm, and for the min-max scaling normalization on average 12.7% of the nodes had an RMSE less than 2 mm. Since the z-score method showed better performance than the min-max scaling on average, it was selected for normalization. The main concept of the z-score is based on calculating the standard deviation of distances of data points from the mean. It aims to have all instances have a mean of zero and a standard deviation of one Roessner et al. (2011). For our problem, this means that the X, Y, and Z coordinates of the nodal positions V of one patient dataset are changed to V_{norm} in which they are centered around the origin (μ) and the standard deviation (σ) of all nodal positions from the origin is one, as shown in equation 1.

$$V_{norm} = \frac{(V - \mu)}{\sigma} \tag{1}$$

2.4. Models

After features generation and data processing, the next step was to build up machine learning models for training. The inputs of the model were the eleven features for the case of the unloaded state estimation, while the 22 features were used for the compression step. The output of the models was the predicted deformation of the instance sequentially starting from step number one till the last desired required step, i.e. the three components of the Euclidean coordinates (X, Y, and Z) of the nodal position belonging to one instance for a particular step. Since our problem is a supervised problem, there are three main approaches: linear model, tree-based models, and artificial neural networks. In this paper, three different models are proposed and compared: two models based on tree-based ensemble models, extremely randomized trees (ERT) similar to the model used in Rupérez et al.

(2018), extreme gradient boosting (XGBoost), and a model based on a recurrent neural network (RNN).

2.4.1. Tree-Based Ensemble Algorithms

The tree-based ensemble algorithm is a subset of tree-based algorithms but is generally considered to be a more accurate model since it is based on building multiple trees together in an ensemble learner, where the features are randomly split in each tree and the predictions of all the trees are combined together. Therefore, the ensemble trees can provide better performance than the traditional tree-based algorithms. Three classes of ensemble learning techniques have been developed for the tree models: bagging, stacking, and boosting. In this paper, we focus on ERT from the family of bagging tree models. It was recently proposed by Martínez-Martínez et al. (2017); Rupérez et al. (2018) which shows the best performance among the three models proposed by them. We also proposed a model from the boosting family which is XGBoost.

Extremely Randomized Tree and Extreme Gradient Boosting The main difference between bagging (ERT) Geurts et al. (2006) and boosting (XGBoost) Chen and Guestrin (2016) is that ERT learns trees independently from each other and in parallel. By that, each model is trained using a different sample from the same training dataset, and the prediction is made by averaging the weak predictions together. Contrary XGBoost learns trees based on the previous one sequentially in an adaptive way. By that each new model is trained based on the performance of the previously trained model and the prediction is made by correcting the error of the previous model. The loss function used for ERT and XGBoost is the root mean square error.

2.4.2. Recurrent Neural Networks

The third model we propose belongs to the family of recurrent neural networks. Recurrent neural networks (RNN) are deep learning algorithms. The main difference between recurrent and neural networks is that they use data from earlier inputs to modify the current input and output. In contrast, conventional neural networks consider inputs and outputs to be independent of one another.

Bidirectional Long Short-Term Memory with an Attention Layer One of the most well-known architectures in RNN is Long short-term memory (LSTM). Each LSTM consists of three main gates: forget gate, input gate, and output gate. The forget gate is the gate responsible for adding or removing information to the cell state, for which the sigmoid function is used Zhou et al. (2016). Bidirectional LSTM memory (BLSTM) processes data in two directions. As a result, this model can use both past and future data. Additionally, there is a layer called the attention layer, which is added as a cascaded layer to the BLSTM. The idea of the attention layer is to apply an activation function to the output to obtain a weighted output vector instead. It consists of two cascaded steps of activation functions. Those activation functions can be, for example, tanh, sigmoid, or Relu. Based on Zhou et al. (2016), Att-BLSTM has a better performance compared to BLSTM without an attention layer.

In this paper, our architecture consists of an encoder and a decoder Luong et al. (2015). The encoder consists of a bidirectional long short-term memory with an attention layer (Att-BLSTM) Zhou et al. (2016). The decoder consists of an LSTM. The loss function for this architecture is also the root mean square.

2.5. Evaluation

In order to evaluate the performance of our proposed models, we considered the deformed nodes from our FEM simulation as the ground truth. By that, we can calculate the root mean square error (RMSE) for each node between our proposed models and the ground truth, as shown in equation 2. In this equation, ϵ represents the deviation of a node's position from the ground truth in the x, y, and z directions. Afterwards, we calculated the mean value of all nodes belonging to one dataset, where one dataset refers to one breast of one patient. Finally, we calculated the mean and median RMSE of all the datasets in the validation set (see section 3).

$$RMSE_{node} = \sqrt{\frac{\epsilon_x^2 + \epsilon_y^2 + \epsilon_z^2}{3}} \tag{2}$$

In addition, we categorized the percentage of nodes from the validation set into classes with an interval of a certain value starting from 0 *mm* to 22 *mm* with a step size of 2 *mm*. Since a few percentages of nodes are located in a class greater than 22 *mm*, we added an additional class for those nodes. This categorization provides a representation of the error distribution.

3. Results

Two groups of datasets were considered in this paper: 26 datasets from the Medical University of Vienna with ages ranging from 29 to 78 years and 232 datasets from the University Hospital of Jena with ages ranging from 23 to 92 years. All datasets were acquired retrospectively. Patients underwent independent normal treatment following the procedures in compliance with relevant laws and institutional guidelines. The collection of data was approved by the institutional committees. Datasets were completely anonymized. Each dataset consisted of a T2-weighted MRI series, which was acquired in clinical practice according to the internal guidelines of the respective hospital. Furthermore, metadata from a corresponding mammogram of the patient was used to parameterize the model, e.g. compression thickness. In total, we used 258 patients. For increasing our database, we first generated breast meshes from both the left and right breast of each patient, resulting in a total of 516 datasets. Second, we extracted intermediate steps between the initial state and the final state of the deformed breast in order to train the model with different deformation states. Since the deformation is a function of time in the FEM simulation

with the dynamic solver, an arbitrary number of intermediate steps could be extracted. To cover a good range of intermediate steps, we extracted 100 steps for the estimation of the unloaded state and around 70 steps for the compression simulation, from the time step when the upper compression plate starts to contact the breast to the time when the breast is fully compressed according to the mammogram's metadata. Since we extract 100 steps for the unloaded state estimation, a total of 70884000 instances could be used for training and validation. Since we extract around 70 steps for the compression step, a total of 48979346 instances is used.

We first applied one-fold validation to optimize the hyperparameters and compare the three models: ERT, XGBoost, and Att-BLSTM. We split our data 90% for the training set (467 datasets) and 10% for the validation set (49 datasets). The validation set has been split equally into 50% of datasets from the Medical University of Vienna and 50% of datasets from the University Hospital of Jena. We investigated the unloaded state estimation and the compression simulation separately.

3.1. Unloaded State Estimation

For the unloaded state estimation, it can be observed from Table 3 that Att-BLSTM provides the minimum mean RMSE of 4.9 *mm*, while the median RMSE for Att-BLSTM and XGBoost is similar when considering the prediction of all 100 intermediate steps. For the last step, the minimum mean RMSE is 6.4 *mm* with Att-BLSTM. Regarding the median, XGBoost works slightly better with a median RMSE of 1.0 *mm* compared to 1.1 *mm* for Att-BLSTM. The standard deviation for both methods is considerably higher due to four and six outliers for XGBoost and Att-BLSTM, respectively. The interquartile range for XGBoost is 2 *mm* and for Att-BLSTM is 1.4 *mm*. Based on the categorization of the percentages of nodes into accuracy classes, as shown in Figure 4, the RMSE values for XGBoost and Att-BLSTM are almost the same.

We visualized two cases in the three views of the body plane: first, a good case is selected based on the minimum error achieved in the Att-BLSTM method to show the performance of our proposed models compared to the deformation from the FEM simulations, as shown in Figure 5, 6, and 7. It is clearly obvious that both methods XGBoost and Att-BLSTM provide visually the same performance with an RMSE of 0.47 *mm* and 0.49 *mm*, respectively, in the three views compared to the FEM simulation (ground truth), while the breast mesh shape predicted by the ERT model with an RMSE of 5.7 *mm* considerably loses volume and the displacement of the nodes does not follow the same pattern as in the displacement estimated by the FEM simulation. Second, for illustration, we also show a case with an RMSE of 5.9 *mm*, 1.1 *mm*, and 1.1 *mm* for ERT, XGBoost, and Att-BLSTM, respectively. In this case, there are some elements erroneously modeled as glandular tissue on the surface of the breast, which is due to a non-optimal automatic segmentation of the MRI volume. Additionally, there are some elements that exceed the quality criterion limits of ABAQUS during the FEM simulation and need to be re-meshed. Despite these challenges in predicting a non-optimal initial dataset, the behavior of the XGBoost and the Att-BLSTM provides visually convincing results, still similar to the deformation in the FEM simulations, as shown in Figure 8, 9, and 10.

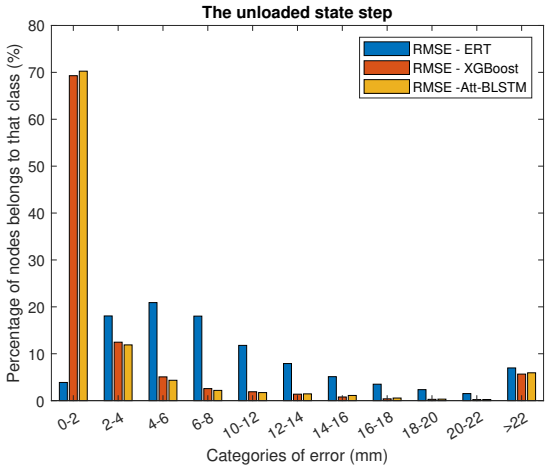

Figure 4: Comparison of the percentage of nodes in each category of error for the unloaded state estimation. The RMSE values were calculated for the three methods (ERT, XGBoost, Att-BLSTM) as an evaluation metric.

To achieve these results, the hyperparameters of the best performing methods XGBoost and Att-BLSTM were empirically optimized using the one-fold validation. For the unloaded state estimation, the XGBoost hyperparameters were set as follows: the number of estimators was set to 55, the learning rate (α) was set to 0.2, the minimum child weight was set to 50, and the maximum depth was set to 6. For Att-BLSTM, the activation function in the attention layer in both stages was set to tanh and Relu, and the learning rate (α) was set to 0.03.

Table 3
Unloaded state estimation - (mean, median) ± standard deviation RMSE (*mm*) in the validation set.

Steps	ERT	XGBOOST	Att-BLSTM
All	(6.8, 5.9) ± 2.9	(6.3, 0.6) ± 36.9	(4.9, 0.6) ± 26.6
Last	(8.1, 6.3) ± 5.5	(7.8, 1.0) ± 37.3	(6.4, 1.1) ± 26.7

3.2. Compression Step

For the compression step, it can be seen from Table 4 that XGBoost provides the minimum mean and median RMSE of 4.9 *mm* and 3.5 *mm* when considering the prediction of all 70 intermediate steps. For the last step, in which the compression is the highest and reaches the compression thickness given in the mammogram's metadata, the mean and median RMSE are 7.3 *mm* and 4.3 *mm* using the XGBoost model. Compared to these values, Att-BLSTM performs slightly worse with an average RMSE of 6.0 *mm* (averaged over all

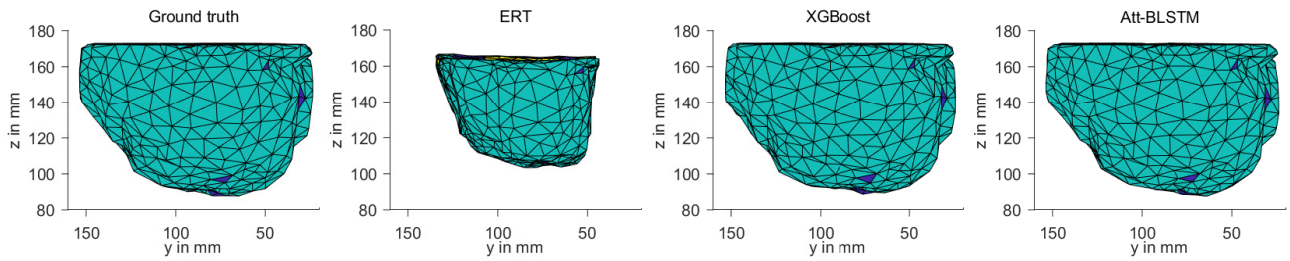

Figure 5: Clinical case with a visually good result in the sagittal plane (lateral view): The comparison of the estimation of the unloaded state between the ground truth (FEM simulation) and the prediction by ERT, XGBoost, and Att-BLSTM. The colors indicate the three-segmented tissues: dark blue is glandular tissue, light blue is fatty tissue, and yellow is muscular tissue.

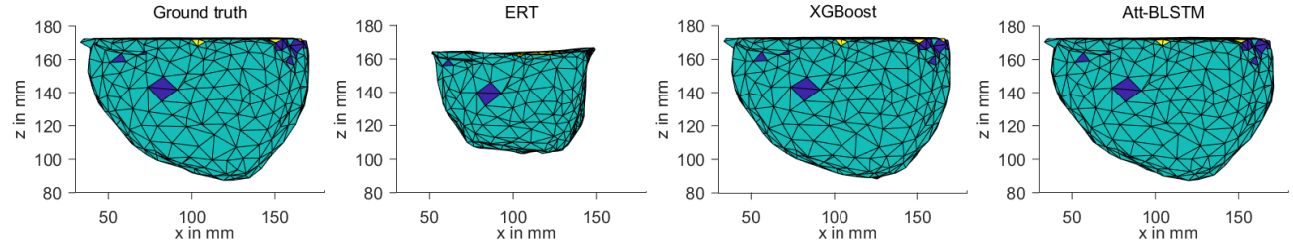

Figure 6: Clinical case with a visually good result in the transversal plane (axial view): The comparison of the estimation of the unloaded state between the ground truth (FEM simulation) and the prediction by ERT, XGBoost, and Att-BLSTM. The colors indicate the three-segmented tissues: dark blue is glandular tissue, light blue is fatty tissue, and yellow is muscular tissue.

steps) and 9.1 *mm* for the full compression step, while ERT performs significantly worse with 10.0 *mm* and 13.4 *mm*, respectively.

Based on the error distribution in Figure 11, it can be observed that Att-BLSTM predicts slightly less nodes with an RMSE higher than 10 *mm* compared to the XGBoost method. The number of nodes with an RMSE lower than 10 *mm* is approximately the same for XGBoost and Att-BLSTM. It can also be realized that there is a significant difference in the first class from $0 - 2\,mm$ and the last class, which summarizes errors greater than 22 *mm*. For the first class, the distribution shows that Att-BLSTM performs slightly better than XGBoost, while the last class indicates that the number of nodes with large error in Att-BLSTM is considerably higher than in XGBoost.

Similar to the unloaded state estimation, we optimized the hyperparameters using the validation set of the one-fold validation. For XGBoost, the number of estimators was set to 80, the minimum child weight was set to 6, the maximum depth was set to 7, and the learning rate (α) was set to 0.08. For Att-BLSTM, the activation function in the attention layer in both stages was set to sigmoid and the learning rate (α) was set to 0.03.

In the following subsections, we emphasize a deeper analysis of the performance of the models with respect to patient characteristics.

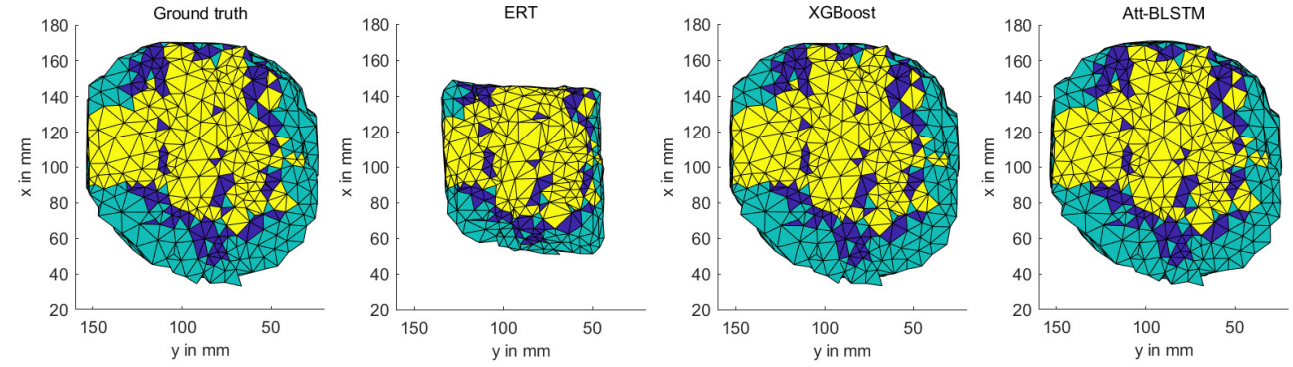

Figure 7: Clinical case with a visually good result in the coronal plane (back view): The comparison of the estimation of the unloaded state between the ground truth (FEM simulation) and the prediction by ERT, XGBoost, and Att-BLSTM. The colors indicate the three-segmented tissues: dark blue is glandular tissue, light blue is fatty tissue, and yellow is muscular tissue.

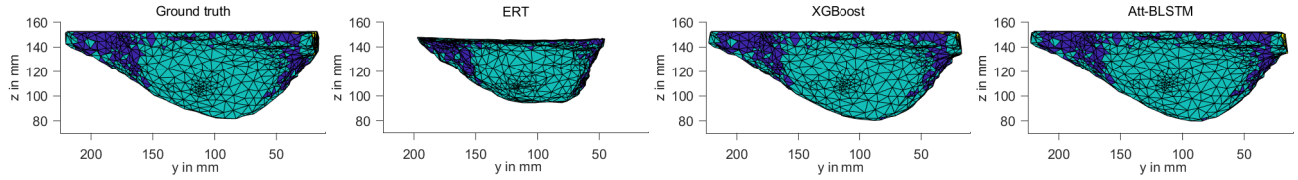

Figure 8: Clinical case with visually non-optimal result in the sagittal plane (lateral view): The comparison of the unloaded state estimation between the ground truth (FEM simulation) and the prediction by ERT, XGBoost, and Att-BLSTM. The colors indicate the three-segmented tissues: dark blue is glandular tissue, light blue is fatty tissue, and yellow is muscular tissue.

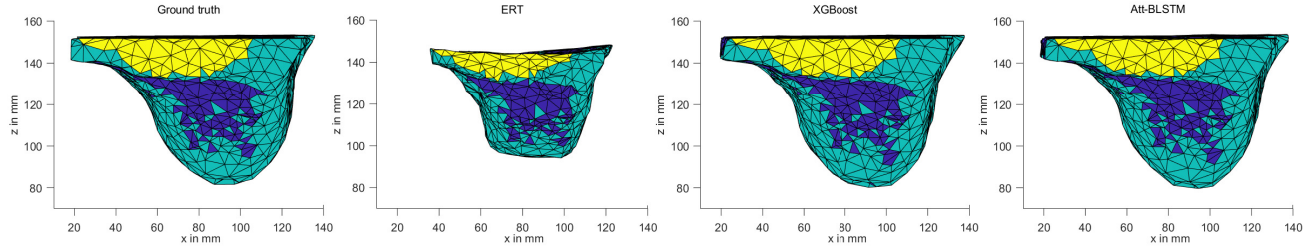

Figure 9: Clinical case with visually non-optimal result in the transversal plane (axial view): The comparison of the unloaded state estimation between the ground truth (FEM simulation) and the prediction by ERT, XGBoost, and Att-BLSTM. The colors indicate the three-segmented tissues: dark blue is glandular tissue, light blue is fatty tissue, and yellow is muscular tissue.

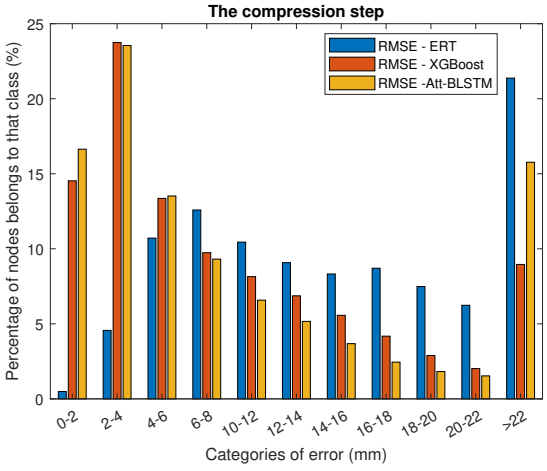

Figure 11: Comparison of the percentage of nodes in each category of error for the compression step. The RMSE values were calculated for the three methods (ERT, XGBoost, Att-BLSTM) as an evaluation metric.

Table 4
Compression step - (mean, median) ± standard deviation RMSE (*mm*) in the validation set

Steps	ERT	XGBOOST	Att-BLSTM
All	(10.0, 8.0) ± 5.4	(4.9, 3.5) ± 4.0	(6.0, 3.6) ± 7.1
Last	(13.4, 10.6) ± 9.9	(7.3, 4.3) ± 7.5	(9.1, 4.7) ± 13.1

3.2.1. Correlation with Features of the Breast

We analyzed our results with respect to three characteristics of the breast: the compression ratio, the error as a function of the different tissue types (glandular, fatty, and muscular tissues), and the breast volume to investigate if subgroups correlate with the RMSE. The analysis was performed based on the validation set of the one-fold validation.

Compression Ratio: Given the difference between the result obtained averaged over all deformation steps and the final step, we hypothesized that the error increases with the compression ratio. To validate our hypothesis, we analyzed a

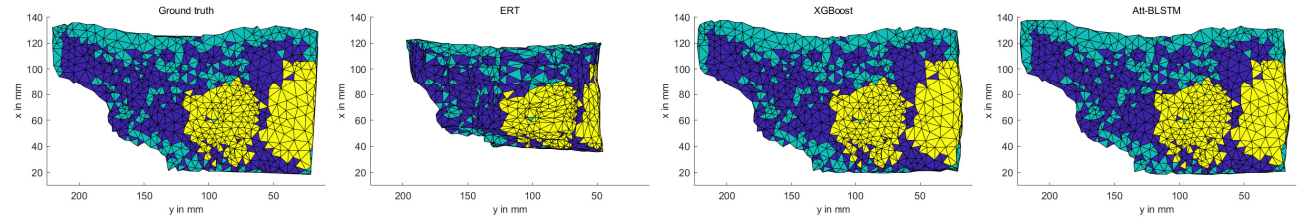

Figure 10: Clinical case with visually non-optimal result in the coronal plane (back view): The comparison of the unloaded state estimation between the ground truth (FEM simulation) and the prediction by ERT, XGBoost, and Att-BLSTM. The colors indicate the three-segmented tissues: dark blue is glandular tissue, light blue is fatty tissue, and yellow is muscular tissue.

correlation between the RMSE and the compression ratio of the validation set (Figure 12) by calculating the compression ratio in the intermediate steps till it reaches the desired breast thickness that is recorded in the metadata for each dataset. We then calculated the mean value for all the datasets at each compression ratio starting from 1% until 76 %, which was the highest compression ratio observed in our patient cohort. The datasets were binned with a step size of 1%. Figure 12 presents the results of this analysis. We applied a second-degree exponential fit to the observed data points. The r-squared of the exponential curve fit is 0.90 for XGBoost, 0.88 for Att-BLSTM, and 0.90 for ERT, which indicates a strong correlation of the fitting curve with the data, thereby confirming our initial hypothesis.

Similarly, we analyzed the correlation between the RMSE and the compression ratio for all the available datasets with 10-fold cross-validation for the XGBoost model, which showed the best results overall, as will be discussed in the next section. The results are shown in Figure 13. The error distribution closely follows the evaluation of the one-fold validation subset. Up to a compression ratio of 53%, it can be realized that the relation between RMSE and the compression ratio increases slowly. In this range, the increase in error with increasing compression ratio can also be considered linear, which we tested by performing a linear fit with an r-squared of 0.93. However, after 53% compression, the error increases considerably, leading us to conclude that the overall error distribution follows an exponential relationship. We also applied a two-degree exponential fitting curve to the 10-fold validation data in Figure, 13, resulting in an r-squared of 0.83.

From the fitted curves in Figure 12, it can again be seen that ERT has the highest error in comparison to the other two methods for all compression ratios but the very highest ones. Furthermore, it can be recognized that both Att-BLSTM and XGBoost perform nearly the same up to a compression ratio of about 53%. At a higher compression ratio, XGBoost shows better results with lower RMSE values compared to Att-BLSTM.

Tissue Type: Second, we analyzed whether there is a relationship between the RMSE and the tissue types considered in our model, i.e. fatty, glandular, and muscular tissues. For this purpose, we subdivided the instances into nodes labeled with the respective tissue type, i.e. the inner nodes of the breast mesh of those elements modeled as fatty, glandular, and muscular tissues. Nodes at the interfaces between tissues are neglected.

For each tissue type, we plotted a histogram of the RMSE for the three models (Figure 14). We fitted a log-normal distribution to the histograms due to the variance in the number of nodes belonging to each class. The μ represents the mean of the logarithmic values of RMSE and the σ represents the standard deviation of the logarithmic values of RMSE. For fatty tissue, XGBoost has the least μ of 1.76 with a mean RMSE of 9.4 *mm*, as shown in Table 5. For glandular tissue, XGBoost has the least μ of 1.7 with a mean RMSE

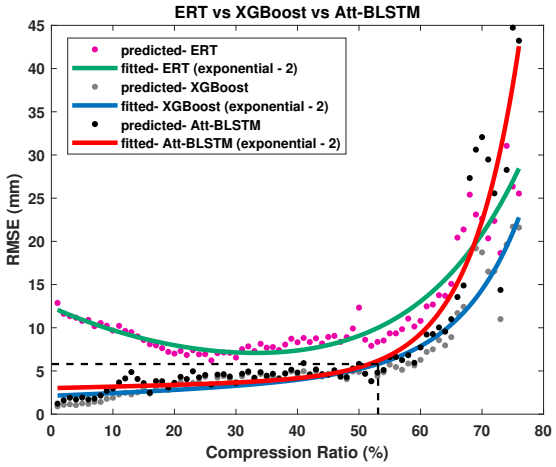

Figure 12: Relation between the compression ratio and the RMSE of the validation set (49 datasets) for the three models: ERT, XGBoost, and Att-BLSTM, respectively. The compression ratio is extracted for every intermediate step for each dataset until it reaches the desired compression ratio extracted from the metadata. The RMSE is the mean of all patients in each intermediate step corresponding to the compression ratio.

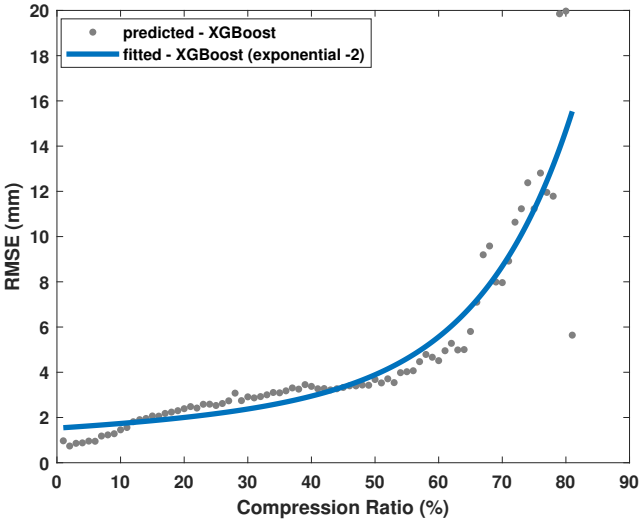

Figure 13: Relation between the compression ratio and the RMSE of the available data with 10-fold cross-validation for the XGBoost model. The representation of compression ratio and RMSE is the same as in Figure 12.

of 8.4 *mm*. For muscular tissue, although Att-BLSTM has the least μ of 1.41, XGBoost has the minimum mean RMSE of 6.5 *mm* and that is because the σ of Att-BLSTM has the highest value of 1.1.

When comparing the different tissue types, there is no obvious trend in all the evaluations, besides that, the RMSE tends to be lower for nodes in muscular tissue than for fatty and glandular tissues. This can be explained by the fact that in our biomechanical model, muscular tissue is modeled as a rigid body that can not deform due to the boundary conditions. Hence it is easier for the machine learning model

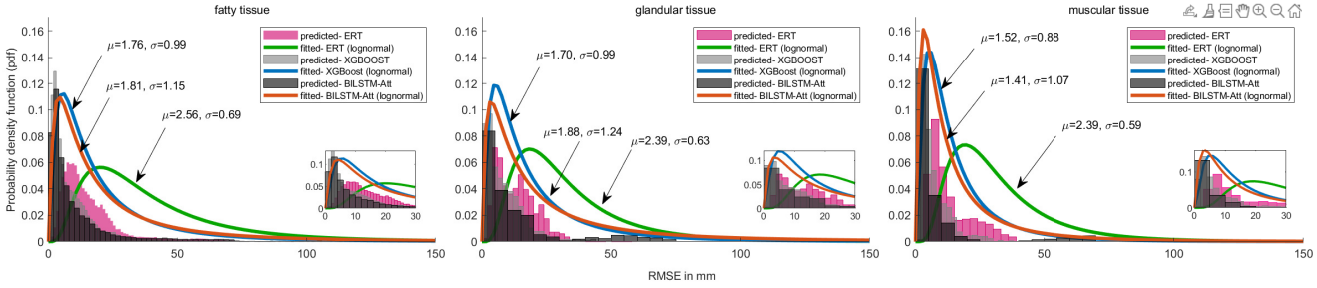

Figure 14: Probability density function versus RMSE: the relation between the tissue type and the RMSE of the validation set for the three models: ERT, XGBoost, and Att-BLSTM.

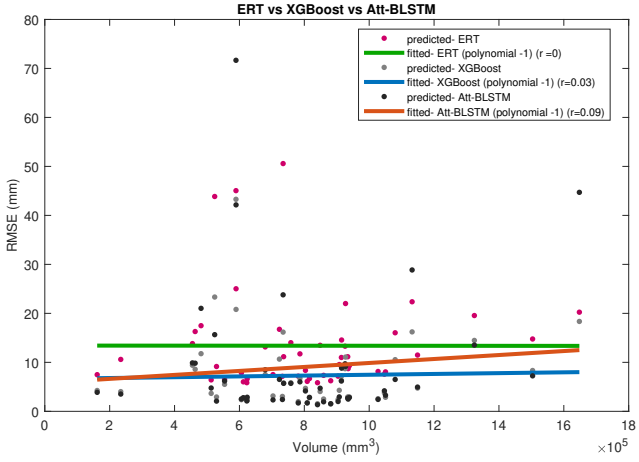

Figure 15: Relation between the breast volume and the RMSE of the validation set for the three models: ERT, XGBoost, and Att-BLSTM. Breast volume has no correlation with the RMSE.

to learn this behavior than the complex deformation of fatty and glandular tissues.

Table 5
Average RMSE for tissues in *mm*

Tissue	ERT	XGBoost	Att-BLSTM
fat	16.6 ± 13.3	**9.4 ± 10.9**	12.1 ± 17.7
glandular	13.1 ± 7.4	**8.4 ± 7.5**	13.3 ± 16.8
muscle	13.1 ± 8.3	**6.5 ± 5.8**	8.4 ± 14.7

Breast Volume: We furthermore investigated whether there is a relationship between the breast volume and the RMSE in order to test if larger breast sizes, which typically deform significantly during mammographic compression, can be predicted with less accuracy as smaller ones. The RMSE was plotted as a function of the breast volume in mm^3 in Figure 15. The data points are widely scattered and no obvious trend is visible. We analyzed the correlation by a polynomial fitting curve with one degree. It is observed that three methods ERT, XGBoost, and Att-BLSTM have an independent relationship with a Pearson correlation coefficient (r) of 0.09 at maximum.

Figures 16, 17, 18, 19, 20, and 21 visualize the same two cases that have been presented for the unloaded state estimation in three views according to three body planes. The first case shows the performance of our proposed models compared to the deformation obtained with the FEM simulation. It is clearly obvious that both methods XGBoost and Att-BLSTM provide similar performance with an RMSE of 1.7 *mm* and 1.7 *mm*, respectively in the three views compared to the FEM simulation (ground truth), while the breast mesh predicted by the ERT method with an RMSE of 6.1 *mm* loses volume and the deformation of the nodes results in a different breast shape as in the FEM simulations. The second case demonstrates a case in which the prediction by neither method provides a visually comparable result. The RMSE in this case is 25 *mm* for ERT, 20.8 *mm* for XGBoost, 42.1 *mm* for Att-BLSTM. This case is considered as one of the cases with a high compression ratio (67%), as the thickness before compression is around 120 *mm*, see Figure 8, and after compression around 40 *mm*, see Figure 19. Additionally, as described earlier, the breast mesh is not optimal, since e.g. glandular tissue can be recognized on the surface of the breast (dark blue), which is a result of a non-optimal automatic segmentation of the MRI. XGBoost fails to represent the shape of the breast and Att-BLSTM not only fails but also leads to a considerable global displacement of the coordinates compared to the ground truth.

3.3. Cross-validation Analysis

As we have demonstrated in the previous sections, XGBoost and Att-BLSTM seem basically to be able to provide a good agreement of predicted breast shapes compared to the FEM ground truth. For the unloaded state estimation, Att-BLSTM and XGBoost show nearly the same results regarding the median RMSE, while XGBoost works better for the compression step given in the one-fold validation.

In order to increase our database and test the methods for over-fitting to the validation set, we applied 10-fold cross-validation for the XGBoost and Att-BLSTM model for the estimation of the unloaded state and the compression step. From Table 7, it can be observed that the average RMSE for XGBoost even decreased to 3.4 *mm* and 4.7 *mm*, respectively. Also, the error distribution was improved significantly for the two simulation steps. The results are furthermore

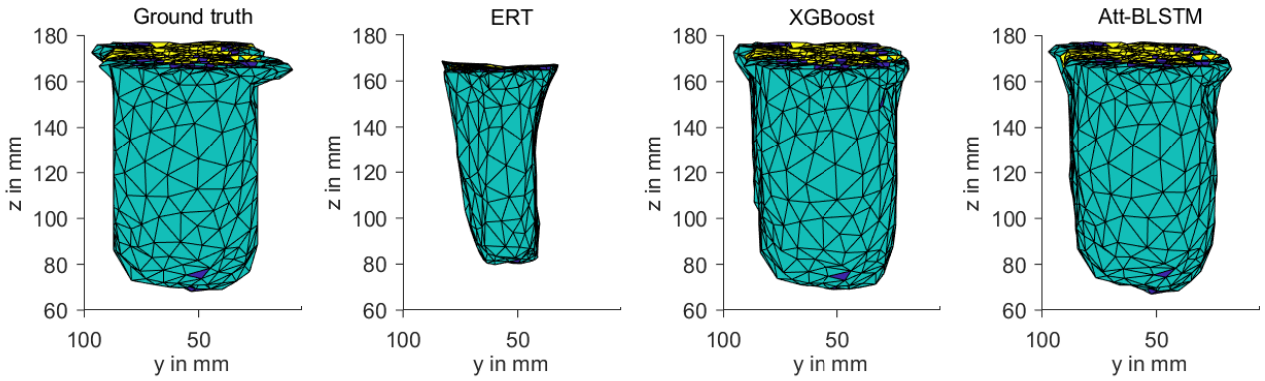

Figure 16: Clinical case with a visually good result in the sagittal plane (lateral view): The comparison of the compression step between the ground truth (FEM simulation) and the prediction by ERT, XGBoost, and Att-BLSTM. The colors indicate the three-segmented tissues: dark blue is glandular tissue, light blue is fatty tissue, and yellow is muscular tissue.

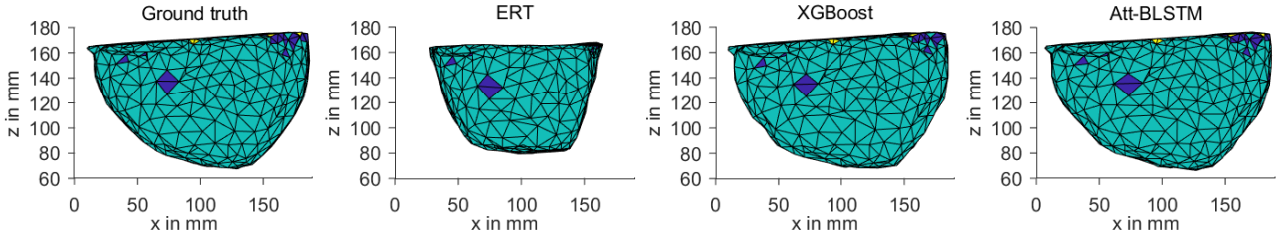

Figure 17: Clinical case with a visually good result in the transversal plane (axial view): The comparison of the compression step between the ground truth (FEM simulation) and the prediction by ERT, XGBoost, and Att-BLSTM. The colors indicate the three-segmented tissues: dark blue is glandular tissue, light blue is fatty tissue, and yellow is muscular tissue.

visualized in Figure 22 and 23. The same was observed for Att-BLSTM with respect to RMSE and error distribution.

From a computation point of view, training our model for XGBoost in a 10-fold cross-validation with the 516 breast meshes took around 4.5 hours, while predicting one dataset takes around 5 seconds. Training Att-BLSTM in a 10-fold cross-validation with 516 breast meshes took around 60 hours, while predicting one dataset takes around 10 seconds on an RTX 2080TI GPU using CUDA 10.2. Compared to a runtime of approximately 20 min for the computation time of a FEM simulation, this comprises a speedup of factor 240 and 120 for XGBoost and Att-BLSTM, respectively. Note that computational optimization of the machine learning method was not the focus of this paper and computation time for prediction may be decreased in the future by explicit performance optimization.

3.4. Comparison to Literature

Martínez-Martínez et al. (2017); Rupérez et al. (2018) achieved an accuracy of 0.62 *mm* for 10 clinical datasets. In comparison, our method for a similar problem in the compression step, achieved a mean and median RMSE of 4.7 *mm* and 3.4 *mm*, respectively for 516 breasts. However, a considerable difference in our work is that a significantly higher compression ratio of up to 76% was used, which leads to huge nonlinear deformations of the breast. Martínez-Martínez et al. (2017); Rupérez et al. (2018) in turn limited their evaluation to a compression thickness of 20%.

At a 20% compression ratio, our methods achieved a mean and median RMSE of 2.3 *mm* and 1.8 *mm*, respectively, with 10-fold cross-validation.

We analyzed two simulation steps, not only the compression step but also, the estimation of the unloaded state. Furthermore, we evaluated our methods using 516 breasts, while the work of Martínez-Martínez et al. (2017); Rupérez et al. (2018) was restricted to 10 phantom and clinical datasets.

We achieved a speedup of approximately a factor of 240 compared to our FEM model simulation. Martínez-Martínez et al. (2017); Rupérez et al. (2018) mentioned the time used for prediction in the ML models, and they mentioned that biomechanical models, in general, could take 120 minutes Hopp et al. (2013); Solves-Llorens et al. (2014) which is approximately a factor of 36000 speedup, as shown in Table 6. Though different modalities were used for breast images, Mendizabal et al. (2019) achieved a speedup by a factor of 130 compared to their FEM model simulation.

4. Discussion and Conclusion

We have presented a machine learning algorithm to simulate the mechanical response of breast tissue when

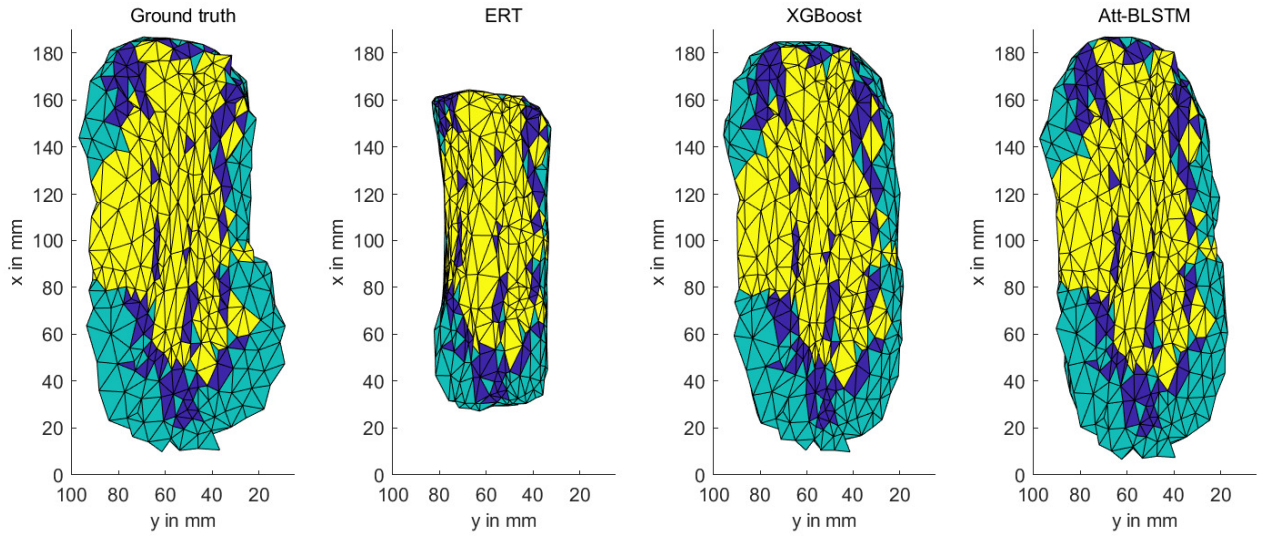

Figure 18: Clinical case with a visually good result in the coronal plane (back view): The comparison of the compression step between the ground truth (FEM simulation) and the prediction by ERT, XGBoost, and Att-BLSTM. The colors indicate the three-segmented tissues: dark blue is glandular tissue, light blue is fatty tissue, and yellow is muscular tissue.

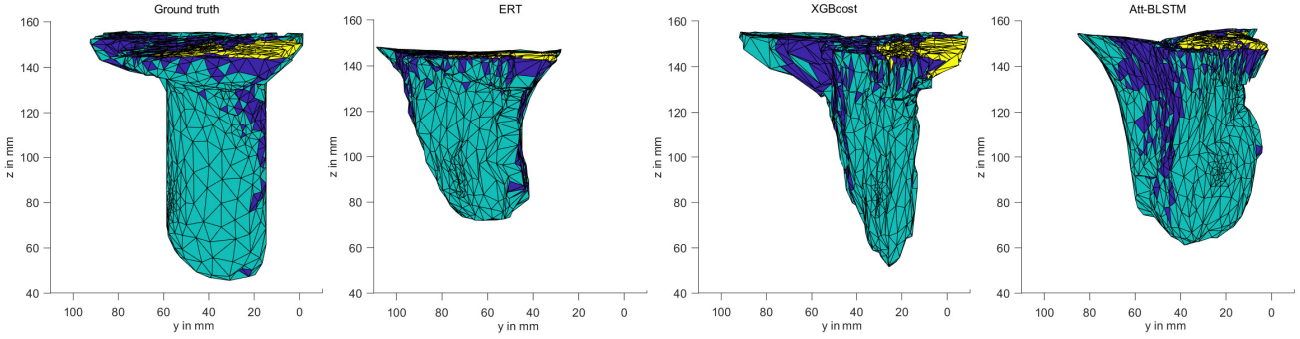

Figure 19: Clinical case with visually non-optimal result in the sagittal plane (lateral view): The comparison of the compression step between the ground truth (FEM simulation) and the prediction by ERT, XGBoost, and Att-BLSTM. The colors indicate the three-segmented tissues: dark blue is glandular tissue, light blue is fatty tissue, and yellow is muscular tissue.

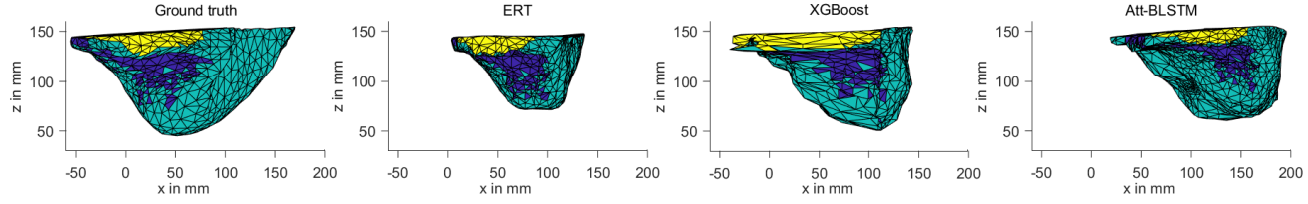

Figure 20: Clinical case with visually non-optimal result in the transversal plane (axial view): The comparison of the compression step between the ground truth (FEM simulation) and the prediction by ERT, XGBoost, and Att-BLSTM. The colors indicate the three-segmented tissues: dark blue is glandular tissue, light blue is fatty tissue, and yellow is muscular tissue.

Table 6
Literature review of machine learning algorithms for breast deformation

Reference	Compression Ratio	Time-FEM	Time-ML	Architecture	#datasets
Martínez-Martínez et al. (2017)	20 %	120 min	<0.2 s	DT/ ERT/RF	Clinical -10
Rupérez et al. (2018)	NA	NA	0.43 s	DT/ERT/RF	Phantom -10
Mendizabal et al. (2019)	NA	407.7 ms	3.14 ms	U-Net	Phantom -10
Said et al.	20 - 76 %	20 min	5 s	ERT/XGBoost/Att-BLSTM	Clinical -516

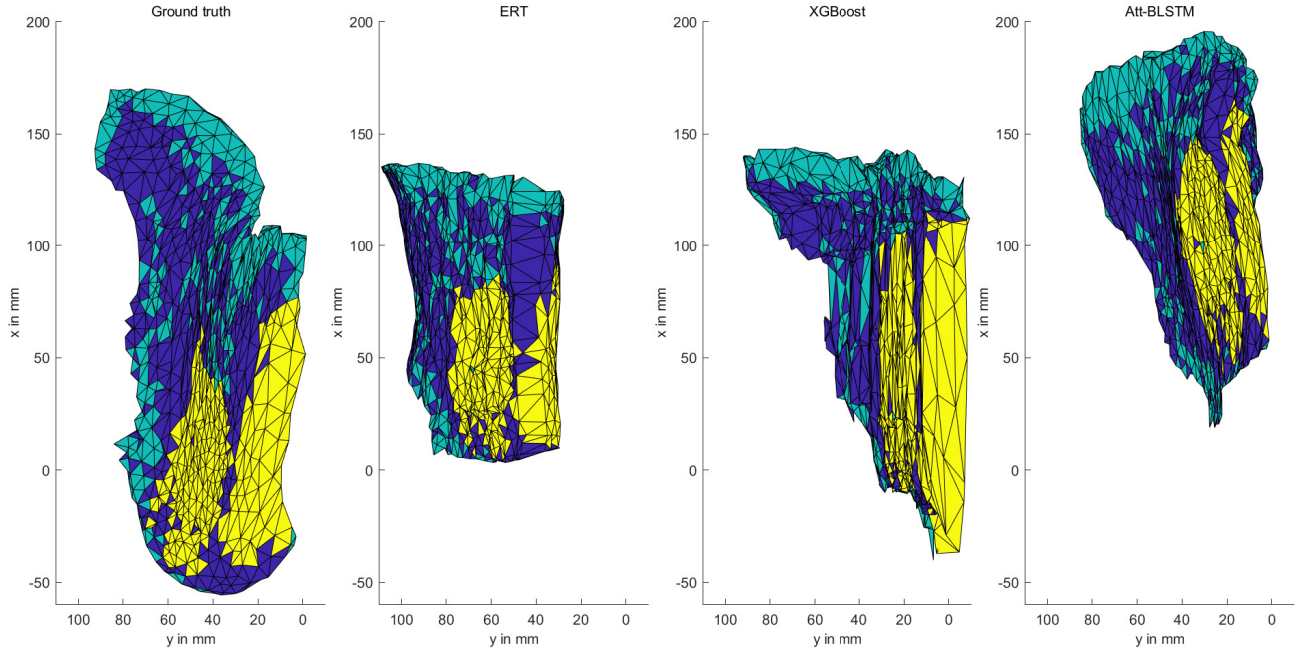

Figure 21: Clinical case with visually non-optimal result in the coronal plane (back view): The comparison of the compression step between the ground truth (FEM simulation) and the prediction by ERT, XGBoost, and Att-BLSTM. The colors indicate the three-segmented tissues: dark blue is glandular tissue, light blue is fatty tissue, and yellow is muscular tissue.

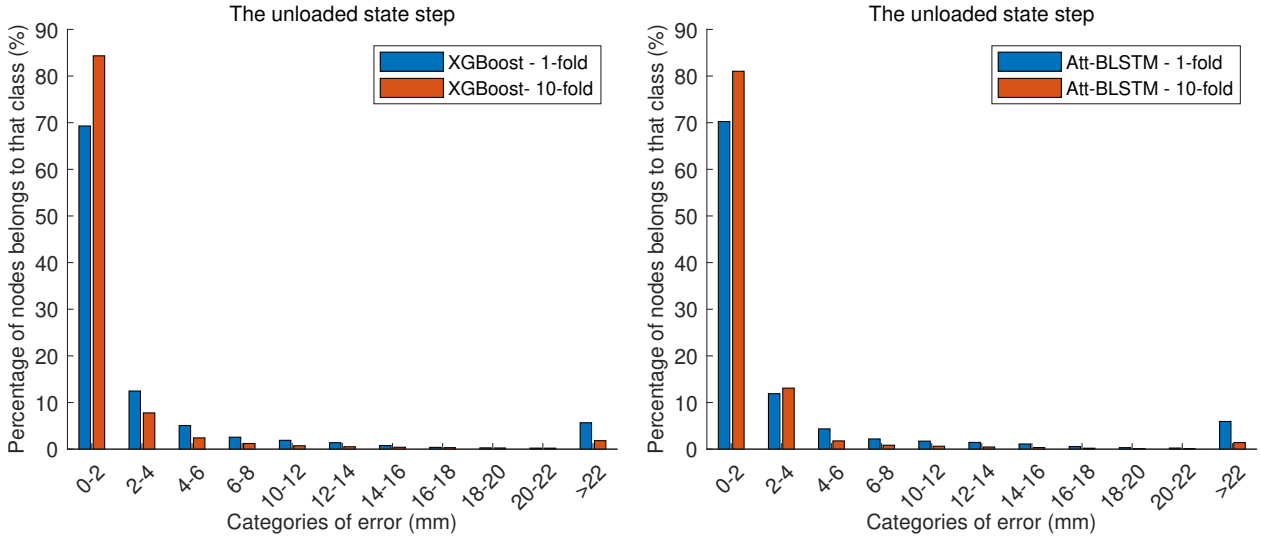

Figure 22: Percentages of nodes split into categories for the unloaded state estimation with XGBoost and Att-LSTM for the 10-fold cross-validation in comparison to the 1-fold cross-validation regarding the RMSE

estimating the unloaded state from a gravity-loaded MRI and when performing a mammographic breast compression. The unloaded state has not previously been predicted by machine learning models in literature. Contrary to literature, in which the compression ratio was only 20%, which is considerably lower than it is usually applied in clinical practice, a significant contribution of this paper is that the methods have been tested with realistic compression ratios and a large number of clinical datasets, thereby covering a variety of breast shapes from clinical routine.

Our methods show very promising results for both the estimation of the unloaded state and the compression simulation with an average RMSE of 3.4 and 4.7 *mm*, respectively.

Although our methods show promising results, there are some limitations to our models. In general, the proposed machine learning and deep learning models have been trained on a very specific biomechanical model. While this model is relatively complex and, as discussed before, has been tested in clinical use cases, the machine learning model obviously

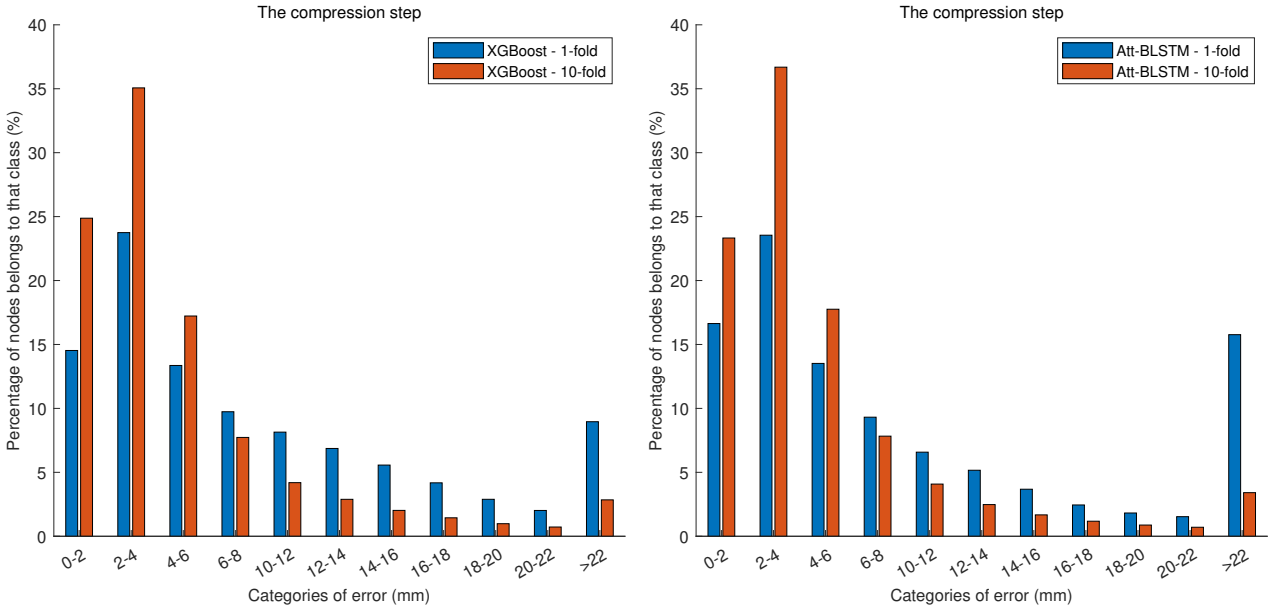

Figure 23: Percentages of nodes split into categories for the compression step with XGBoost and Att-LSTM for the 10-fold cross-validation in comparison to the 1-fold cross-validation regarding the RMSE

Table 7
RMSE ((mean, median) ± standard deviation) of 10-fold cross-validation for the unloaded state estimation and the compression step in the last step for XGBoost and Att-BLSTM.

Method	Unloaded state	Compression
XGBoost	**(3.4, 0.8) ± 30.5 mm**	**(4.7, 3.4) ± 4.7 mm**
Att-BLSTM	**(3.0, 1.2) ± 22.3 mm**	**(4.9, 3.4) ± 5.6 mm**

can not be generalized to considerable changes in the biomechanical model. For example, the model was trained with a certain resolution of the finite element mesh. Predicting the deformation for finer or coarser meshes may lead to different results. Furthermore, meshes not fulfilling certain quality criteria as they are e.g., checked by ABAQUS, may lead to different results. Similarly, for the material parameters of tissues, we restricted training and testing to constant values from literature. Such material properties could be added in the future as a free parameter for the model in order to allow better generalization for other FEM use cases.

We performed a cross-validation analysis to avoid overfitting problems with more than 500 cases in total. The patient cohort included a variety of breast shapes and sizes from clinical routine and images from two different clinical sites. It has to be considered that the machine learning and deep learning model have been trained for the realistic compression applied to the particular patient during X-ray mammography, thereby the total number of cases with a very high compression ratio is small compared to the number of cases with lower compression ratios. This may have led to an exponential increase in the error at very high compression ratios. In order to generalize better in the future, we would like to enhance the datasets that have a compression ratio of more than 60%. Furthermore, our method may be tested with more unseen datasets in the future to improve statistics and generalization.

Also, we would like to add more experiments (mesh grid search) for finetuning the hyperparameters and analyzing different loss functions for the three models.

From the analysis of the relationship between compression ratio and error, we can conclude that the XGBoost and Att-BLSTM models work stable up to a compression ratio of approximately 53%. Moreover, we found out that there is no dependence on breast volume, which is considered a good sign since it is common for large breasts to have strong deformation during mammographic compression.

Establishing the proposed methods may be a considerable step to replace FEM simulations describing the deformation of the breast subject to mammographic compression. This would significantly speed up the process from approximately 20 minutes to approximately 5 seconds in our case and thereby lead to clinically relevant computation time. Besides, it will open the possibility to increase the optimization space for biomechanically informed image registration considerably, since some image registration approaches like Hopp et al. (2012) require an optimization process for parameters such as rotation angle around axes, compression thickness, and Young's moduli of the different tissues. For each iteration to optimize parameters, a FEM simulation will take 20 minutes. In turn with the machine learning and deep learning models, several rotations, compression thickness, and Young's moduli can be tried out in a fraction of a minute which is expected to increase the registration accuracy.

5. Acknowledgments

This work was funded by the German Research Foundation (DFG) under grant number 5565/3-1 and the Austrian Science Fund (FWF) under grant number 4240.

References

Azar, F., Metaxas, D., Schnall, M., 2000. A finite element model of the breast for predicting mechanical deformations during biopsy procedures, in: Proceedings IEEE Workshop on Mathematical Methods in Biomedical Image Analysis. MMBIA-2000 (Cat. No.PR00737), pp. 38–45. doi:10.1109/MMBIA.2000.852358.

Chen, T., Guestrin, C., 2016. Xgboost: A scalable tree boosting system, in: Proceedings of the 22nd ACM SIGKDD International Conference on Knowledge Discovery and Data Mining, Association for Computing Machinery, New York, NY, USA. p. 785–794. URL: https://doi.org/10.1145/2939672.2939785, doi:10.1145/2939672.2939785.

Chung, J., Rajagopal, V., Nielsen, P.M.F., Nash, M., 2008. A biomechanical model of mammographic compressions. Biomechanics and modeling in mechanobiology 7, 43—52. URL: https://doi.org/10.1007/s10237-006-0074-6, doi:10.1007/s10237-006-0074-6.

Dietzel, M., Baltzer, P.A., Hopp, T., Ruiter, N.V., Kaiser, W.A., 2012. Co-registration of MR-mammography and X-ray mammography. European Journal of Radiology 81, S27–S29. URL: https://www.sciencedirect.com/science/article/pii/S0720048X12700116, doi:https://doi.org/10.1016/S0720-048X(12)70011-6. extended abstracts and Abstracts of the Sixth International Congress on MR-Mammography.

Dietzel, M., Hopp, T., Ruiter, N.V., Kaiser, C.G., Kaiser, W.A., Baltzer, P.A., 2015. 4D co-registration of X-ray and MR-mammograms: initial clinical results and potential incremental diagnostic value. Clinical Imaging 39, 225–230. URL: https://www.sciencedirect.com/science/article/pii/S089970711400271X, doi:https://doi.org/10.1016/j.clinimag.2014.11.003.

Fang, Q., Boas, D.A., 2009. Tetrahedral mesh generation from volumetric binary and grayscale images, in: 2009 IEEE International Symposium on Biomedical Imaging: From Nano to Macro, pp. 1142–1145. doi:10.1109/ISBI.2009.5193259.

García, E., Diez, Y., Diaz, O., Lladó, X., Gubern-Mérida, A., Martí, R., Martí, J., Oliver, A., 2019. Breast MRI and X-ray mammography registration using gradient values. Medical Image Analysis 54, 76–87. URL: https://www.sciencedirect.com/science/article/pii/S1361841519300179, doi:https://doi.org/10.1016/j.media.2019.02.013.

García, E., Diez, Y., Diaz, O., Lladó, X., Martí, R., Martí, J., Oliver, A., 2018. A step-by-step review on patient-specific biomechanical finite element models for breast MRI to X-ray mammography registration. Medical Physics 45, e6–e31. URL: https://aapm.onlinelibrary.wiley.com/doi/abs/10.1002/mp.12673, doi:https://doi.org/10.1002/mp.12673, arXiv:https://aapm.onlinelibrary.wiley.com/doi/pdf/10.1002/mp.12673.

Geurts, P., Ernst, D., Wehenkel, L., 2006. Extremely randomized trees. Mach. Learn. 63, 3–42. URL: https://doi.org/10.1007/s10994-006-6226-1, doi:10.1007/s10994-006-6226-1.

Han, L., Hipwell, J.H., Eiben, B., Barratt, D., Modat, M., Ourselin, S., Hawkes, D.J., 2014. A nonlinear biomechanical model based registration method for aligning prone and supine MR breast images. IEEE transactions on medical imaging 33, 682—694. URL: https://doi.org/10.1109/TMI.2013.2294539, doi:10.1109/tmi.2013.2294539.

Han, L., Hipwell, J.H., Tanner, C., Taylor, Z., Mertzanidou, T., Cardoso, J., Ourselin, S., Hawkes, D.J., 2011a. Development of patient-specific biomechanical models for predicting large breast deformation. Physics in Medicine and Biology 57, 455–472. URL: https://doi.org/10.1088/0031-9155/57/2/455, doi:10.1088/0031-9155/57/2/455.

Han, L., Hipwell, J.H., Tanner, C., Taylor, Z., Mertzanidou, T., Cardoso, J., Ourselin, S., Hawkes, D.J., 2011b. Development of patient-specific biomechanical models for predicting large breast deformation. Physics in Medicine Biology 57, 455. URL: https://dx.doi.org/10.1088/0031-9155/57/2/455, doi:10.1088/0031-9155/57/2/455.

Hipwell, J.H., Vavourakis, V., Han, L., Mertzanidou, T., Eiben, B., Hawkes, D.J., 2016. A review of biomechanically informed breast image registration. Physics in Medicine and Biology 61, R1–R31. URL: https://doi.org/10.1088/0031-9155/61/2/r1, doi:10.1088/0031-9155/61/2/r1.

Hopp, T., Baltzer, P., Dietzel, M., Kaiser, W.A., Ruiter, N.V., 2012. 2D/3D image fusion of X-ray mammograms with breast MRI: visualizing dynamic contrast enhancement in mammograms. International journal of computer assisted radiology and surgery 7, 339—348. URL: https://doi.org/10.1007/s11548-011-0623-z, doi:10.1007/s11548-011-0623-z.

Hopp, T., Cotič Smole, P., Ruiter, N., 2017. Automated Multimodal Breast CAD Based on Registration of MRI and Two View Mammography, pp. 365–372. doi:10.1007/978-3-319-67558-9_42.

Hopp, T., Dietzel, M., Baltzer, P., Kreisel, P., Kaiser, W., Gemmeke, H., Ruiter, N., 2013. Automatic multimodal 2D/3D breast image registration using biomechanical FEM models and intensity-based optimization. Medical Image Analysis 17, 209–218. URL: https://www.sciencedirect.com/science/article/pii/S136184151200148X, doi:https://doi.org/10.1016/j.media.2012.10.003.

Hopp, T., Neupane, B., Ruiter, N.V., 2016. Automated Multimodal Computer Aided Detection Based on a 3D-2D Image Registration, in: Tingberg, A., Lång, K., Timberg, P. (Eds.), Breast Imaging, Springer International Publishing, Cham. pp. 400–407.

Lee, A.W., Rajagopal, V., Babarenda Gamage, T.P., Doyle, A.J., Nielsen, P.M., Nash, M.P., 2013. Breast lesion co-localisation between X-ray and MR images using finite element modelling. Medical Image Analysis 17, 1256–1264. URL: https://www.sciencedirect.com/science/article/pii/S1361841513000856, doi:https://doi.org/10.1016/j.media.2013.05.011.

Liu, Y.L., Liu, P.Y., Huang, M.L., Hsu, J.T., Han, R.P., Wu, J., 2017. Simulation of breast compression in mammography using finite element analysis: A preliminary study. Radiation Physics and Chemistry 140, 295–299. URL: https://www.sciencedirect.com/science/article/pii/S0969806X17300774, doi:https://doi.org/10.1016/j.radphyschem.2017.01.017. 2nd International Conference on Dosimetry and its Applications (ICDA-2) University of Surrey, Guildford, United Kingdom, 3-8 July 2016.

Luong, M., Pham, H., Manning, C.D., 2015. Effective approaches to attention-based neural machine translation. CoRR abs/1508.04025. URL: http://arxiv.org/abs/1508.04025, arXiv:1508.04025.

Martínez-Martínez, F., Rupérez-Moreno, M., Martínez-Sober, M., Solves-Llorens, J., Lorente, D., Serrano-López, A., Martínez-Sanchis, S., Monserrat, C., Martín-Guerrero, J., 2017. A finite element-based machine learning approach for modeling the mechanical behavior of the breast tissues under compression in real-time. Computers in Biology and Medicine 90, 116–124. URL: https://www.sciencedirect.com/science/article/pii/S0010482517303177, doi:https://doi.org/10.1016/j.compbiomed.2017.09.019.

Mendizabal, A., Tagliabue, E., Brunet, J.N., Dall'Alba, D., Fiorini, P., Cotin, S., 2019. Physics-based Deep Neural Network for Real-Time Lesion Tracking in Ultrasound-guided Breast Biopsy, in: Computational Biomechanics for Medicine XIV, Shenzhen, China. URL: https://hal.inria.fr/hal-02311277.

Mertzanidou, T., Hipwell, J., Johnsen, S., Han, L., Eiben, B., Taylor, Z., Ourselin, S., Huisman, H., Mann, R., Bick, U., Karssemeijer, N., Hawkes, D., 2014. MRI to X-ray mammography intensity-based registration with simultaneous optimisation of pose and biomechanical transformation parameters. Medical Image Analysis 18, 674–683. URL: https://www.sciencedirect.com/science/article/pii/S1361841514000358, doi:https://doi.org/10.1016/j.media.2014.03.003.

Miller, K., Joldes, G., Lance, D., Wittek, A., 2006. Total lagrangian explicit dynamics finite element algorithm for computing soft tissue deformation. Communications in Numerical Methods in Engineering 23, 121 – 134. doi:10.1002/cnm.887.

Moreira, P., Peterlík, I., Herink, M., Duriez, C., Cotin, S., Misra, S., 2013. Modelling prostate deformation: Sofa versus experiments. Mechanical Engineering Research 3, 64–72.

Pasciak, J.E., 1995. The mathematical theory of finite element methods (Susanne c. brenner and l. Ridgway Scott). SIAM Review 37,

472–473. URL: https://doi.org/10.1137/1037111, doi:10.1137/1037111, arXiv:https://doi.org/10.1137/1037111.

Phellan, R., Hachem, B., Clin, J., Mac-Thiong, J.M., Duong, L., 2021. Real-time biomechanics using the finite element method and machine learning: Review and perspective. Medical Physics 48, 7–18. URL: https://aapm.onlinelibrary.wiley.com/doi/abs/10.1002/mp.14602, doi:https://doi.org/10.1002/mp.14602, arXiv:https://aapm.onlinelibrary.wiley.com/doi/pdf/10.1002/mp.14602.

Roessner, U., Nahid, A., Chapman, B., Hunter, A., Bellgard, M., 2011. 1.33 - metabolomics – the combination of analytical biochemistry, biology, and informatics, in: Moo-Young, M. (Ed.), Comprehensive Biotechnology (Second Edition). second edition ed.. Academic Press, Burlington, pp. 447–459. URL: https://www.sciencedirect.com/science/article/pii/B9780080885049000520, doi:https://doi.org/10.1016/B978-0-08-088504-9.00052-0.

Ruiter, N., Müller, T., Stotzka, R., Gemmeke, H., Reichenbach, J., Kaiser, W., 2002. Automatic image matching for breast cancer diagnostics by a 3D deformation model of the mamma 47, 644–647. URL: https://doi.org/10.1515/bmte.2002.47.s1b.644, doi:doi:10.1515/bmte.2002.47.s1b.644.

Ruiter, N., Stotzka, R., Muller, T.O., Gemmeke, H., Reichenbach, J., Kaiser, W., 2006. Model-based registration of X-ray mammograms and MR images of the female breast. IEEE Transactions on Nuclear Science 53, 204–211. doi:10.1109/TNS.2005.862983.

Rupérez, M.J., Martínez-Martínez, F., Martínez-Sober, M., Lago, M.A., Lorente, D., Bakic, P.R., Serrano-López, A.J., Martínez-Sanchis, S., Monserrat, C., Martín-Guerrero, J.D., 2018. Modeling the mechanical behavior of the breast tissues under compression in real time, in: Tavares, J.M.R., Natal Jorge, R. (Eds.), VipIMAGE 2017, Springer International Publishing, Cham. pp. 583–592.

Said, S., Clauser, P., Ruiter, N.V., Baltzer, P.A.T., Hopp, T., 2021. Image registration between MRI and spot mammograms for X-ray guided stereotactic breast biopsy: preliminary results, in: Linte, C.A., Siewerdsen, J.H. (Eds.), Medical Imaging 2021: Image-Guided Procedures, Robotic Interventions, and Modeling, International Society for Optics and Photonics. SPIE. p. 115981C. URL: https://doi.org/10.1117/12.2581820, doi:10.1117/12.2581820.

Said, S., Meyling, M., Huguenot, R., Horning, M., Clauser, P., Ruiter, N.V., Baltzer, P.A.T., Hopp, T., 2022. MRI breast segmentation using unsupervised neural networks for biomechanical models, in: Bosmans, H., Marshall, N., Ongeval, C.V. (Eds.), 16th International Workshop on Breast Imaging (IWBI2022), International Society for Optics and Photonics. SPIE. p. 122860C. URL: https://doi.org/10.1117/12.2624245, doi:10.1117/12.2624245.

Samani, A., Bishop, J., Yaffe, M., Plewes, D., 2001. Biomechanical 3-D Finite Element Modeling of the Human Breast using MRI Data. IEEE Transactions on Medical Imaging 20, 271–279. doi:10.1109/42.921476.

Si, H., Gärtner, K., 2005. Meshing piecewise linear complexes by constrained delaunay tetrahedralizations, in: Hanks, B.W. (Ed.), Proceedings of the 14th International Meshing Roundtable, Springer Berlin Heidelberg, Berlin, Heidelberg. pp. 147–163.

Siegel, R.L., Miller, K.D., Fuchs, H.E., Jemal, A., 2022. Cancer statistics, 2022. CA: A Cancer Journal for Clinicians 72, 7–33. URL: https://acsjournals.onlinelibrary.wiley.com/doi/abs/10.3322/caac.21708, doi:https://doi.org/10.3322/caac.21708.

Smith, M., 2009. ABAQUS/Standard User's Manual, Version 6.9. Dassault Systèmes Simulia Corp, United States.

Solves-Llorens, J., Rupérez, M.J., Monserrat, C., Feliu, E., García, M., Lloret Larrea, M., 2014. A complete software application for automatic registration of x-ray mammography and magnetic resonance images. Medical Physics 41, 1–10. doi:10.1118/1.4885957.

Tanner, C., Schnabel, J.A., Hill, D.L.G., Hawkes, D.J., Leach, M.O., Hose, D.R., 2006. Factors influencing the accuracy of biomechanical breast models. Medical Physics 33, 1758–1769. URL: https://aapm.onlinelibrary.wiley.com/doi/abs/10.1118/1.2198315, doi:https://doi.org/10.1118/1.2198315, arXiv:https://aapm.onlinelibrary.wiley.com/doi/pdf/10.1118/1.2198315.

The CGAL Project, 2022. CGAL User and Reference Manual. 5.5.1 ed., CGAL Editorial Board. URL: https://doc.cgal.org/5.5.1/Manual/packages.html.

Wellman, P.S., Howe, R.D., Kern, K.A., 1999. Breast tissue stiffness in compression is correlated to histological diagnosis.

Zhou, P., Shi, W., Tian, J., Qi, Z., Li, B., Hao, H., Xu, B., 2016. Attention-based bidirectional long short-term memory networks for relation classification, in: Proceedings of the 54th Annual Meeting of the Association for Computational Linguistics (Volume 2: Short Papers), Association for Computational Linguistics, Berlin, Germany. pp. 207–212. URL: https://aclanthology.org/P16-2034, doi:10.18653/v1/P16-2034.

Zienkiewicz, O., Taylor, R., Zhu, J., 2013. Chapter 10 - incompressible problems, mixed methods, and other procedures of solution, in: Zienkiewicz, O., Taylor, R., Zhu, J. (Eds.), The Finite Element Method: its Basis and Fundamentals (Seventh Edition). seventh edition ed.. Butterworth-Heinemann, Oxford, pp. 315–359. URL: https://www.sciencedirect.com/science/article/pii/B9781856176330000101, doi:https://doi.org/10.1016/B978-1-85617-633-0.00010-1.